An injected quantity estimation technique based on time–frequency analysis

An injected quantity estimation technique based on time-frequency analysis

Ferrari Alessandro (*),1, Jin Zhiru[1], Vento Oscar[1] and Zhang Tantan[1]

[1]*Energy Department*

Politecnico di Torino, Corso Duca degli Abruzzi 24, 10129, Torino, Italy

(*) Corresponding author. Email: alessandro.ferrari@polito.it   Phone +390110904426

1. Abstract

An innovative injected quantity estimation method, based on time-frequency analysis, has been developed for passenger car Common-Rail (CR) injection systems. This method involves capturing the pressure time history from a transducer installed along the rail-to-injector pipe, and its overall accuracy has been found to be within 1.5 mg.

The dependence of the injected mass on the fuel temperature has been investigated, and the correlation of the injected mass with the nominal rail pressure and the energizing time has been evaluated for different thermal regimes. It has been verified that if the duration of the hydraulic injection is considered instead of the energizing time, the influence of the temperature on the injected mass is implicitly taken into account. Thus, the corresponding correlations between the injected mass and the duration of the hydraulic injection have been obtained for different nominal rail pressures.

The duration of the hydraulic injection has been measured through an effective time-frequency analysis technique, which has been used to realize a virtual sensor of the needle lift.

The experimental campaign has been performed over a wide range of working conditions for single injections, and the accuracy of the innovative prediction methodology, which can be exploited to design a closed-loop control of the injected mass, has been assessed.

2. Keywords

Common-rail, time-frequency analysis, injected mass estimation, fuel injection system

3. Highlights

- A correlation between the injection temporal length and injected mass is obtained.
- Nozzle opening and closure are detected by means of a virtual needle-lift sensor.
- The injected mass is predicted from a pressure trace measured at the injector inlet.

1. Introduction

Internal combustion engines require continuous development [1], due to the demand for improved performances with increased fuel economy and in order to comply with stringent emission legislations [2, 3]. In addition to the design of new technologies, researchers have been focusing on fault detection and diagnosis of the system [4, 5, 6] to fulfill these requirements.

In-cylinder pressure measurements and analyses have played important roles in the field of diagnosis and real time monitoring [7, 8]. The main features of the combustion process can be identified and evaluated by analyzing an accurately processed pressure signal. Investigations of this kind include the detection and control of the start of combustion [9, 10], of the heat release rate [11] as well as of knock and misfire phenomena [12, 13]. Similarly, empirical models have been established to determine the ignition delay [14] and the barycenter of combustion [15].

Time-frequency analysis (TFA), a powerful tool that may be used to analyze non-stationary signals [16], has been applied to detect and diagnose machinery faults [17, 18]. This advanced technique has also been proposed to study combustion and knock in diesel engines by evaluating the vibration signals in these engines [6, 19]. Among the various techniques that are available, short-time Fourier transform (STFT) is generally applied to characterize signals in the time-frequency domain. It is possible, for example, to estimate such characteristic combustion parameters as the peak combustion pressure and peak pressure rise rate through the vibration signal [20]. An estimation of the trapped mass was carried out in [21, 22] by means of an analysis of the in-cylinder pressure resonance.

The detection of vibration sources, by means of STFT, was proposed in [23] for mechanical systems. The main events of an injection, that is, the opening and the closure of the nozzle, were identified in [24] by analyzing the pressure signal from a diesel engine fuel injection apparatus.

One topic of great interest in the real-time monitoring of diesel engines is related to the accurate control of the mass injected into diesel injection systems. Different advanced compensative strategies have been set up by injection apparatus suppliers: i-ART, presented by Denso [25], NCS, proposed by Bosch [26] and the Switch technology by Delphi [27]. With these techniques, semi-empirical correlations or transfer functions are implanted in the electronic control unit (ECU), and specific signals are captured and used to estimate the injected quantity. The nominal rail pressure (p_{nom}) or the energizing time (*ET*) can then be compensated for by comparing the estimated injected mass value and the target value. However, such compensative strategies can only ensure an improvement in the accuracy of the injected mass for those engine working conditions for which the correlations fit. In fact, the usage of a transfer function is not founded on a physical basis, since the injector cannot be modeled by means of ordinary differential equations of time invariant coefficients. In general, one of the main drawbacks of engine calibrations of the injected mass is represented by the thermal regime: the calibrations are usually prepared with the injection system installed on the hydraulic rig under certain temperature conditions, and they can result inaccurate for many thermal regimes experienced in the engine. This is the main discrepancy that requires compensation. On the one hand, a reliable and accurate correction of the injected mass, with respect to the thermal regime of the engine, is very difficult to realize. On the other hand, such a correction could lead to clear benefits, in terms of the reduction in soot (6%), NO_x (3÷4%) engine out emissions and CO_2, as well as in combustion noise (as much as 5 dB) and fuel consumption [28, 29].

In the present work, a new correlation has been developed between the injected mass, the nominal rail pressure and the injection temporal length (*ITL*) to design a robust, original, closed-loop control of the injected mass. *ITL* has been determined by means of a previously developed, TFA-based, virtual sensor of the needle lift [24]. The introduction of *ITL* into the correlation allows the thermal regime of the injector to be included in the prediction of the injected mass.

2. Time-frequency analysis

TFA integrates the techniques that study signals in both the time and the frequency domains in order to indicate the changes in the frequency spectrum of a transient signal $f(t)$. In the present work, the focus has been on the changes in the nozzle opening and closure instants. A great number of fast Fourier transforms (FFT) are performed over consecutive, overlapping, short-time ranges, and each FFT result refers to the mean instant of the time interval. The non-stationary signal is assumed to refer to a stationary performance within each time interval, and a local frequency spectrum is therefore obtained. From an operative point of view, a windowing of signal $f(t)$ is carried out: signal $f(t)$ is multiplied by a selected window function $h(t-\tau)$, which is of unit energy and is only non-zero over an interval around instant τ. The short-time Fourier transform (STFT) is then evaluated as follows:

$$F(\nu,\tau) = \int_{-\infty}^{+\infty} f(t) \cdot h(t-\tau) e^{-j2\pi\nu t} dt \tag{1}$$

Since the selected window function does not introduce any energy variation, the energy density spectrum P_f of signal f is obtained in the following way:

$$P_f(\nu,\tau) = |F(\nu,\tau)|^2 \tag{2}$$

The energy of signal f, denoted as E_f, is given by

$$E_f = \int_{-\infty}^{+\infty} \int_{-\infty}^{+\infty} P_f(\nu,\tau) d\tau d\nu \tag{3}$$

The energy density spectrum P_f can be interpreted as a probability density function to evaluate the following mean instantaneous frequency (*MIF*):

$$\bar{\nu}(\tau) = \frac{1}{\int_{-\infty}^{+\infty} P_f(\nu,\tau) d\nu} \int_{-\infty}^{+\infty} \nu \cdot P_f(\nu,\tau) d\nu \tag{4}$$

Hence, the *MIF* can be interpreted as the most representative frequency of a signal at a certain time instant.

3. Experimental setup

The experimental campaign has been conducted on a Moehwald-Bosch hydraulic test bench installed in the ICE laboratory at the Politecnico di Torino. The bench is capable of providing a nominal power of 35 kW, a maximum torque of 100 Nm and a maximum speed of 6100 rpm. As reported in Fig. 1, the injection rate and the injected quantity that refer to the injector under analysis were captured by means of a Zeuch method-based flowmeter (HDA from Moehwald-Bosch) [30]. The electric current supplied to the injector was measured by means of a current clamp. Furthermore, one piezoresistive pressure transducer was mounted along the rail-to-injector pipe of the CR system in order to acquire the pressure time history at the electroinjector inlet (p_{inj}). Finally, a PXI (from National Instruments) was connected to the output of the pressure transducer in order to collect p_{inj} at a sample frequency of 500 kHz.

A state-of-the-art Bosch fuel injection system for passenger cars has been tested. A high-pressure rotary pump, with a double-effect single piston and a total displacement of 430 mm^3/rev, is employed in the system. Bosch CRI 2.18 solenoid-actuated injectors (cf. Fig. 2), which feature a pressure balanced pilot-valve at the exit of the control chamber, were installed.

A schematic of the hydraulic circuit of the injection system from the rail onward is reported in Fig. 3. When the injection system is operating, high-pressure fuel, supplied by the pump to the rail, enters the injector through a rail-to-injector pipe. A small quantity of the fuel arrives in the control chamber (cf. V_{cc} in Fig. 3), while the rest fills the delivery chamber, located upstream of the injection holes. When the electrical current is supplied to the solenoid, the pilot-valve is open and the fuel pressure in the control chamber reduces, because of the fuel recirculated to the tank. The needle ascends, due to an imbalance of the pressure forces that act on its working surfaces, and the nozzle opens, thus allowing the fuel to be injected through the injection holes. When the current is shut down by the ECU, the closure of the pilot-valve makes the pressure rise in the control chamber, and this results in a downstroke of the needle. As soon as the needle arrives at its initial position, the injection holes close again.

Shell V-Oil 1404 (ISO 4113) calibration fluid is employed at the hydraulic test bench, because it reproduces the physical properties of diesel oil over an adequate pressure and temperature range.

Tests were carried out considering single injections, featuring p_{nom} over the 500-1700 bar range, and ET over the 0.35-1.1 ms range, with oil temperatures, measured at the fuel tank, equal to either T_{tank}=40 °C or 68 °C.

All the experimental tests of the present work were conducted at a fixed pump speed of 2000 rpm, which corresponds to an engine speed of 2000 rpm (the pump-to-engine speed ratio is 1:1). Since the pump speed does not exert any significant influence on the CR performance, the obtained results can be generalized to other engine speeds.

4. Injector characteristics

Figure 4 reports the values of the injected mass, measured by means of the HDA flowmeter, as an average of 100 consecutive engine cycles for different p_{nom} and ET. The temperature of the fuel in the tank (T_{tank}) was set either at 40 °C (cf. circle symbols and dashed lines) or at 68 °C (cf. square symbols and continuous lines). In fact, diesel fuel injection system suppliers usually assume a reference temperature of 40 °C for hydraulic tests. Furthermore, the 68 °C value corresponds to the maximum temperature that can be reached on the current test bench (a limit of around 70 °C is common on hydraulic test benches for safety reasons). The M_{inj} versus ET curves for each T_{tank} and p_{nom} value are fitted by a third-order polynomial. The fuel velocity through the nozzle can in fact be considered a function of p_{nom} and T_{tank}, and the same occurs for the density. Since the restricted flow area at the nozzle is a quadratic function of the needle lift and the needle-lift peak value can be considered to grow proportionally with ET (the needle is ballistic and the needle lift time history has a triangular shape), the mean injected flow-rate can be regarded as a quadratic polynomial function of ET at fixed p_{nom} and T_{tank} and the injected mass as a cubic function of ET at fixed p_{nom} and T_{tank}. Figure 5 reports the trend of the mean injected flow-rate, namely $\overline{G_{inj}}$, with respect to ET for three different nominal rail pressures at T_{tank} = 40 °C (the polynomial coefficients of the interpolating curves are listed in the graph). As can be inferred, the experimental data of $\overline{G_{inj}}$ correlate well with quadratic polynomials and the contribution of the second order term is not marginal compared to the contribution of the linear term.

The injected mass grows as T_{tank} increases under fixed p_{nom} and ET values. Furthermore, the lower the rail pressure is, the higher the difference between the injected masses when T_{tank} is changed. Figs. 6a and 6b report some ET sweeps of injected mass flow-rate (G_{inj}) patterns pertaining to p_{nom}=800 bar and p_{nom}=1600 bar, respectively. G_{inj} time histories at T_{tank}=40 °C and 68 °C are compared in each graph. The injected flow-rate at p_{nom} = 800 bar is controlled more by the needle seat passage than at p_{nom} = 1600 bar. In fact, the higher ET in Fig. 6a is, the higher the needle lift peak value and the higher the injected flow-rate peak value; this does not occur at p_{nom} = 1600 bar (cf. Fig. 6b), where the flow-rate is mainly controlled by the nozzle injection holes and therefore, independently of the peak value of the needle lift, which increases with ET (the injector is ballistic), the maximum G_{max} value remains constant. All this justifies a greater impact of the needle lift time history on the injected flow rate time history, when p_{nom}=800 bar. Since a temperature increase determines a reduction in the fuel viscosity [31] and a subsequent diminution in the friction stresses [32] acting on the needle, the thermal effect on the injected mass is more obvious at p_{nom}=800 bar than at p_{nom}=1200 bar or p_{nom}=1600 bar. From the comparison of the data obtained at T_{tank}=40°C and T_{tank}=68°C, it has been possible to analyze sufficiently the investigated effect: the predominant effect of the fuel temperature on the injector dynamics is the reduced friction force acting on the needle and this is in line with what determined in [33] for higher injector inlet temperatures than 0 °C.

It can be observed, from the data reported in Fig. 4, that when p_{nom}=800 bar and ET=800 µs are applied (M_{inj}≈25 mg at T_{tank}=40°C), the difference in the injected quantity between the two considered temperatures of the fuel in the tank can reach a value close to 3 mg. Furthermore, the injection temperature variation can generally be higher when the injection system, installed on the engine, undergoes different thermal regimes than when it is tested at the hydraulic rig, first at T_{tank}= 40 °C and then at T_{tank}= 68 °C.

Accurately determining thermal regimes in the nozzle of an injector during operations on an engine is a complex procedure [34]: the fuel temperature at the injector inlet grows, in comparison to T_{tank}, at a rate of about 1 °C for every 100 bar of pump compression, and most of the temperature increase occurs through the injector. However, for the purpose of the present analysis, it was sufficient to characterize the thermal regime with the controllable temperature of the fuel in the tank. Indeed, the injected flow-rate is sensitive to T_{tank}. The start of injection (*SOI*) occurs at almost the same time instant as T_{tank} changes (cf. Figs. 5a and 5b), but the flow-rates pertaining to the lower temperature start to decrease earlier, thereby advancing the end of injection (*EOI*). *ITL* can be expressed as

$$ITL = EOI - SOI \tag{5}$$

which is the time interval during which the instantaneous injected flow-rate G_{inj} is higher than zero, as indicated in Fig. 6 with reference to ET = 700 µs (for other ET values ITL is defined in the same way). It is observed that for increasing T_{tank}, ITL enlarges. As a consequence, when p_{nom} is fixed and the fuel temperature rises, the correlation between the injected mass and ET shifts, in line with the data shown in Fig. 4.

Third-order polynomial fitting of the ITL-M_{inj} data was conducted for each p_{nom} and the correlations are plotted in Fig. 7. As can be inferred, the correlation between ITL and M_{inj} remains for fixed p_{nom} as T_{tank}

varies from 40 °C to 68 °C. Thus, it can be observed that the ITL-M_{inj} correlation is almost independent of the fuel temperature. This suggests the possibility of determining M_{inj} on the basis of the experimental p_{nom} and ITL values, independently of T_{tank}, which leads to a more robust correlation than the common one implemented on the ECU, namely $M_{inj}=f(ET, p_{nom})$.

5. Implementation of the TFA injection duration sensor

Figure 8 shows the G_{inj}, p_{inj} and the energizing current traces pertaining to p_{nom}=1200 bar and ET =600 µs. The reported traces correspond to average values over 100 consecutive engine cycles. No obvious residual pressure waves are present in the hydraulic circuit before the injection starts: therefore, $p_{inj}(t)$ remains almost horizontal. As the energizing current is activated, a slight reduction in p_{inj} takes place, due to the opening of the pilot-valve and, as soon as the effective injection starts (*SOI*), an expansion wave is triggered, and this causes a significant decrease in p_{inj} (marked 1 in Fig. 8). The stimulated rarefaction waves are reflected at the rail and propagate backward and forward along the rail-to-injector pipe, and this results in fluctuations of p_{inj} with respect to the time. The amplitude of the p_{inj} oscillations remains pronounced over the entire injection phase, although they are gradually damped by wall friction along the rail-to-injector pipe and by concentrated losses. As soon as the hydraulic injection phase finishes (*EOI*), the closure of the nozzle induces a water hammer with an evident rise and final peak in p_{inj} (event marked 2 in Fig. 8).

The time instants that refer to the important changes in p_{inj} (cf. 1 and 2 in Fig. 8) are linked to the corresponding hydraulic events (*SOI* and *EOI*). However, the determination of the exact time instant at which the decrease in p_{inj} pertaining to *SOI* really starts is not an easy task, since any pressure disturbing variation can affect the detection. Similar problems are encountered for the determination of *EOI*. In fact, reflected pressure waves traveling along the rail-to-injector pipe can influence the p_{inj} time history, thus making the capture of the *EOI* misleading.

TFA can be a useful tool to apply to p_{inj} in order to extract well-resolved information on *SOI* and *EOI* for the estimation of the final injected mass. In general, the *SOI* and the *EOI* of the same injector are concentrated within a time span of 4 ms. In order to locate those time instants with TFA and to avoid any leakage errors (these are given by spurious harmonic terms that are generated when only a portion of a periodic signal is considered [35]), ascribable to the start and the end of the signal, a sequence of $p_{inj}(t)$ frames, each with a total length of 8 ms, has been taken as the signal on which *MIF* is evaluated.

In order to smooth the experimental p_{inj} signal, it was preliminarily treated with a Butterworth low-pass filter of the fourth order with a cut-off frequency of 50 kHz. The thus processed signal, namely $p_{inj,fil}$, was used to substitute $f(t)$ in Eq. (1). A Hanning window was selected as the window function employed in Eq. (1):

$$h(n) = 0.5 \left(1 - \cos\left(2\pi \frac{n}{N}\right)\right), 0 \leq n \leq N \tag{6}$$

where n stands for a discretized time instant in the window, and N+1 is the window length (duration) in terms of number of samples. In the present work, a window length of 502 μs was chosen. Provided that the sample frequency of p_{inj} is 500 kHz, N will be equal to 251. By applying these parameters and conditions, the STFT of p_{inj} is obtained via Eq. (1), and *MIF* can then be calculated by means of Eqs. (2) and (4).

It must be noticed that the sample frequency may be reduced around 20 kHz without any criticism. This value is able to contain almost all the energy content of the pressure signal frequency spectrum [36], leading to a remarkable reduction of the computational time.

6. Results

Figures 9-11 plot the electrical current, as well as the G_{inj}, p_{inj} and *MIF* time histories for three different working conditions of p_{nom} and *ET* over a time interval of 4 ms, where T_{tank} was set to 40 °C. The MIF trace in the plots takes on a constant value before the electrical start of the injection has occurred, but this initial level is not visible in the graphs because it is a too large value, due to the leakage error.

By analyzing the *MIF* trace referring to the pressure at the injector inlet, the main impulsive events regarding the injection can be detected. The *MIF* time history is sensitive to the needle movements, and both the beginning of its ascendent phase (when the injection starts) and the end of the descending phase (when the injection ends) can be identified with high resolution as quick changes in the *MIF* value. The first local maximum in the *MIF* diagram (related to nozzle opening, marked as 1 in Figs. 9-11) can be estimated as the hydraulic start of injection (*SOI*), which takes place around 0.1 ms after the effective instant at which the nozzle opens, and G_{inj} thus becomes higher than zero (cf. Figs. 9-11). Such a delay is necessary for the rarefaction wave that is triggered by the injection to propagate from the nozzle to the pressure transducer location [24]. Similarly, the time instant at which the absolute maximum value of *MIF* (related to the water hammer at the end of the injection event) occurs, that is, at about 0.1 ms after the end of the hydraulic injection, was considered as the *EOI*. It has been seen that this criterion holds for all the working points examined in the experimental campaign for both T_{tank} = 40 °C and T_{tank} = 68 °C.

The *MIF* estimated injection duration (ITL_{est}) and the real one, namely *ITL*, were in turn calculated by means of Eq. (5), and with the corresponding experimental data referring to *MIF* and injected flow rate, respectively. Since similar delays occur at both the start and the end of ITL_{est}, *ITL* and ITL_{est} can be considered as coincident. As can be inferred from the legends in Figs. 9 and 10, the errors between ITL_{est} and *ITL* are1.49 µs and 5.71 µs, respectively (percentage errors below 1%).

Figure 11 plots the same quantities as those shown in Figs. 9 and 10 for the p_{nom}=600 bar and *ET*= 1000 µs case. The instants, estimated as *SOI* and *EOI* with the support of *MIF*, feature a time delay of around 0.18 ms with respect to the real values. However, when the G_{inj} trace is considered, the error between *ITL* and ITL_{est} is 90.74 µs, which is much higher than in Figs. 9 and 10. This alteration occurs for very large ET values and may be due to the superposition of the rail reflected waves and the water hammer along the rail-to-injector pipe (*ET* = 1000 µs is not usually applied for this injector setup).

The calculated ITL_{est} data shown in Fig. 9 and Fig. 10 were applied to the correlation reported in Fig. 7, and values of the estimated injected mass ($M_{inj,est}$) equal to 30.84 mg and 16.01 mg were predicted, respectively. If a comparison with the corresponding M_{inj} data evaluated by means of the HDA flowmeter is made, the errors in the prediction of the injected mass are well below 0.5 mg, which can be considered a very satisfactory result. For the case in Fig. 11, $M_{inj,est}$ is 27.56 mg and there is a difference of 1.2 mg, compared to the M_{inj} value of the HDA flowmeter.

The estimated injected mass has been evaluated for various steady-state working conditions, in terms of p_{nom} and *ET*, by means of the developed correlation, based on the TFA methodology. The modulus of the difference between $M_{inj,est}$ and M_{inj}, that is, the prediction accuracy $|\Delta M_{inj}|$, is reported as the vertical ordinate in the 3D diagrams in Fig. 12 as a function of p_{nom} and *ET*. The fuel temperature, T_{tank}, was set at 40 °C (cf. Fig. 12a) and at 68 °C (cf. Fig. 12b). The M_{inj} values were measured, by means of the HDA flowmeter, and they correspond to average values of over 100 consecutive engine cycles. Since the maximum injected mass per engine cycle is below 45 mg for the considered application involving these injectors, the range over which both p_{nom} and ET were high was excluded from the experimental campaign. The accuracy is generally within 1 mg for over 80% of the explored working conditions. $|\Delta M_{inj}|$ can reach values close to 1.5 mg for either 500 bar $\leq p_{nom} \leq$ 600 bar and medium and high ET values with T_{tank} at both 40 °C and 68 °C or for 350 µs $\leq ET \leq$450 µs and high p_{nom} values when T_{tank} is equal to 40 °C. The injected mass percentage errors under the two considered fuel temperature values have also been evaluated and are reported in Fig. 13 (cf. Fig. 13a for T_{tank} = 40 °C and Fig. 13b for T_{tank} = 68 °C). When the injected masses are small for both the fuel tank temperatures, a small absolute error (even if it is smaller than 1 mg) can lead to a percentage error up to 15%, which is an acceptable value. Preliminary tests were also performed on double injections (pilot-main injections). In such a case, it is difficult to evaluate *ITL,* due to the numerous events that affect p_{inj}, especially when the dwell time between the consecutive injections is reduced. The present methodology can be used to control the mass injected during the first pilot injection of the multiple injection train, and this can lead to benefits in terms of reductions in soot and NO_x engine out emissions, as well as in combustion noise. Similarly, the strategy could be applied to control the main fuel shot of a main-after injection schedule.

6. Discussion

The new applied transfer function appears to be more simple and direct than the compensative strategies mentioned in Sect. 1, where different steps are required: based on a measured pressure signal, the needle lift is deduced and this outcome is then used in the prediction of the injected flow-rate, which is finally integrated to estimate the injected mass. The presented technique is not invasive from the injector point of view, it can be applied to different injector types without any modification in the injector internal layout.

It is worth observing that there are two contributions to the $|\Delta M_{inj}|$ error. The first is the error introduced by the correlation; although the fitting technique is satisfactory, with an accuracy within 0.5 mg, this contribution is not negligible for state-of-the-art injection systems. The second contribution, which is the predominant one, is the error in the estimation of *ITL* due to the superposition of the pressure waves. The injected flow rate not only depends on the rail pressure (which is controlled in the *CR* system), but also on the needle dynamics. The latter aspect is only taken into account roughly in standard engine calibrations, because they make use of *ET*, which, as has been shown, can differ significantly from the effective injection duration. The implementation of the correlation between the injected mass and *ITL* for different p_{nom} on the engine ECU maps improves the consistency of the M_{inj} interpolation model, because *ITL* is more closely related to the needle lift than *ET*. Furthermore, the application of *ITL* as an independent variable of the correlation allows the thermal effect of the injector to be included in the prediction of the injected mass: this is a fundamental point, as may be observed in Fig. 4, since the thermal regime significantly influences the injected mass at fixed values of *ET* and p_{nom}.

From the injector characteristics (cf. Fig. 4), at T_{tank}= 40°C, the injected mass is smaller than 3 mg for $p_{nom} \leq 800$ bar and *ET* = 350 μs (for a pilot injection the injected mass is usually below this value). Under these working conditions, the percentage error on the fuel estimated mass with the closed loop control is below 15% (cf. Fig. 13) for both 40°C and 68°C (this is an optimum value for injected masses below 10 mg), while this error can arrive at 25% if the temperature increase from 40°C to 68°C and an open-loop control is adopted. Furthermore, if a low temperature combustion is considered, the pilot injected quantity can be increased till 7-8 mg [37]: in this case, the percentage error on the M_{inj} estimation at T_{tank}= 68°C is in the 2%-15% range (cf. Fig. 13), while becomes higher than 30% for the open loop control. In this way, in the presence of a multiple injection strategy, the injected mass control could be implemented to the first pilot injection. Moreover, further efforts are needed to accurately filter the *MIF* time history, in order to remove the disturbances due to pressure waves, and to be able to efficiently apply the procedure to multiple injections with reduced dwell times. This represents a possible future step in the development of the new control strategy. In addition, the same strategy could be applied to control the late phased post injection for DPF regeneration.

Figure 14 reports the scheme of a possible closed-loop control strategy based on the presented technique, that could be applied cycle-by-cycle. The *ITL* is estimated based on the measured $p_{inj,in}$ through the TFA virtual sensor. The *ITL* estimation and the nominal rail pressure level p_{nom} can then be used to evaluate the injected mass ($M_{inj,est}$). Such a value is compared with the injected mass target ($M_{inj,ref}$), stored in the *ECU* maps and the difference, namely $\varepsilon = M_{inj,ref} - M_{inj,est}$, is the input value to a *PID* controller in order to correct the *ET* value sent to the injector. The determined correction can be applied to the next injection cycle.

In [28,29], it has been proved the effectiveness of the application of a feedback signal to correct the *ET* in order to mitigate the error led by the thermal regime of the engine. As has been already assessed [28], a closed-loop control of the injected mass, based on cycle-to-cycle *ET* correction, is generally able to maintain the repeatability of the fuel dosage achieved under a standard open-loop strategy, that is below 10% for all the considered cases for a state-of-the-art injector [28]. In other words, the proposed closed loop should improve the accuracy of the injected mass without affecting its precision. It is challenging to improve the elevated precision of the open-loop control because it is based on the severe tolerances applied to the injector manufacturing process and, moreover, the closed loop control is more aimed at compensating physical effects (due to thermal regime) than cycle-to-cycle dispersion (due to stochastic phenomena). In order to achieve the latter objective, the accuracy of the *ITL* vs. M_{inj} correlation should be further improved (the error should be below 0.5 mg), but this appears a difficult task.

The actual technology would in principle need a pressure sensor placed near to each injector inlet along the rail-to-injector pipes (contrarily to the strategies presented in [28,29], where two sensors are required). However, since the differences in M_{inj} are due to the injector thermal regime and are therefore based on a physical phenomenon, the same correction, evaluated for one injector, can be applied to the other injectors by taking into account the injector-to-injector dispersion. The latter is considered in the *ECU* maps by means of special injector codes that further correct the nominal *ET* for each injector. Hence, a single pressure sensor applied at the inlet of one of the injectors is expected to be enough for the multi-cylinder engines.

7. Conclusions

A closed-loop control of the injected mass would be a valuable innovation for designing cleaner and more efficient diesel engines.

A method for a real-time estimation of the injected mass has been designed by applying a TFA technique to the pressure time history measured at the injector inlet and the reliability of the method has been assessed on single injections.

The dependence of the injected mass on the thermal regime of the injector has been preliminarily investigated by varying T_{tank} at fixed p_{nom} and *ET*: the difference in the corresponding injection rate patterns is mainly related to *ITL*. When p_{nom} is fixed and *ITL* is employed as the controlled variable instead of *ET*, an accurate correlation of M_{inj} can be obtained with *ITL*, which is independent of T_{tank}.

A TFA-based virtual sensor of the needle lift, which was presented in a previous work, has then been assessed and further developed in order to estimate the *ITL*. The *MIF* trace, obtained from the pressure signal measured at the injector inlet, is the key to capturing the two time instants that are used to obtain ITL_{est}. The injection duration is evaluated by monitoring the first *MIF* peak after the energizing current (which is related to the nozzle opening) and the absolute maximum of the *MIF* (related to the water hammer at the end of the injection event). Hence, thanks to these points, ITL_{est} can be determined.

Finally, the $M_{inj,est}$=$M_{inj,est}$ (p_{nom}, ITL_{est}) correlations have been used to predict the injected mass for an extended working condition range of the injection system (in terms of p_{nom}, *ET* and T_{tank}): for single injections, the observed accuracy of the algorithm results to be below 1.5 mg for all the considered cases, and within 1 mg for most of them. Two different sources of error affect the injected mass estimation: the first is related to the *ITL*-M_{inj} correlation and the second is associated with the inaccuracy of ITL_{est}.

The presented method can be applied to design a closed-loop control strategy of the injected mass for single injections or to control the mass injected during the first injection of a multiple injection schedule. This can help to minimize the well-known inaccuracy that can be observed when a calibration conducted at a hydraulic bench is used in the engine, where different thermal conditions can be experienced. A scheme for the implementation of the closed loop control has been reported: difference $M_{inj,ref}$- $M_{inj,est}$ is used as an input value to a PID controller in order to correct the *ET* of the next injection cycle.

8. Nomenclature

CR Common Rail

E	signal energy
ET	energizing time
ECU	electronic control unit
EOI	end of injection
FFT	fast Fourier transform
FMV	fuel metering valve
G	mass flow-rate
h	window function
ITL	injection temporal length
n	discretized time instant
M	fuel mass
MIF	mean instantaneous frequency
P	energy density spectrum
p	fuel pressure
PCV	pressure control valve
P/E	pressure sensor
SOI	start of injection
STFT	short-time Fourier transform
T	fuel temperature
t	time
TFA	time-frequency analysis
ε	error on the injected mass
ν	frequency
τ	time

Subscripts

0	reference
cc	control chamber

est estimated

inj injected, injector

nom nominal

tank tank

9. References

[1] BS. Dooren, C. Balerna, M. Salazar, A. Amstutz, C. Onder, Optimal Diesel Engine Calibration using Convex Modelling of Pareto Frontiers, *Control Engineering Practice* 96 (2020) 104313.

[2] Z. Liu, A. DizqahS, J. Herreros, J. Schaub, O. Haas, Simultaneous Control of NOx, Soot and Fuel Economy of a Diesel Engine with Dual-loop EGR and VNT Using Economic MPC, *Control Engineering Practice* 108 (2021) 104701.

[3] E. A. El Shenawy, Medhat Elkelawy, Hagar Alm-Eldin Bastawissi, Hitesh Panchal, Mahmoud M. Shams, Comparative study of the combustion, performance, and emission characteristics of a direct injection diesel engine with a partially premixed lean charge compression ignition diesel engines, *Fuel* 249 (2019) 277-285.

[4] X. Chen, L. Liu, J. Zhang, J. Du, A Signal Processing of In-Cylinder Pressure for the Resonant Frequency Prediction of Combustion Process in Diesel Engines, ASME 2018 Internal Combustion Engine Division Fall Technical Conference, Volume 2: Emissions Control Systems; Instrumentation, Controls, and Hybrids; Numerical Simulation; Engine Design and Mechanical Development, ICEF2018-9534, San Diego, California, USA, November 4-7, 2018.

[5] J. Daniel, Y. Kok, F. Erik, K. Mattias, Combining Model-based Diagnosis and Data-driven Anomaly Classifiers for Fault Isolation, *Control Engineering Practice* 80 (2018) 146-156.

[6] A. Taghizadeh-Alisaraei, A. Mahdavian, Fault Detection of Injectors in Diesel Engines Using Vibration Time-frequency Analysis, *Applied Acoustics* 143 (2019) 48-58.

[7] C. Guardiola, B. Pla, P. Bares, A. Stefanopoulou, Cylinder Charge Composition Observation Based on In-cylinder Pressure Measurement, *Measurement* 131 (2019) 559-568.

[8] J. Zhao, J. Wang, On-Board Fuel Property Identification Method Based on High-Pressure Common Rail Pressure Signal, *Journal of Dynamics Systems, Measurement and Control* 136-3 (2014) 031010.

[9] F. Cheng, M. Ouyang, F. Yang, Real-time Start of Combustion Detection Based on Cylinder Pressure Signals for Compression Ignition Engines, *Applied Thermal Engineering* 114 (2017) 264-270.

[10] Joseph Gerard T. Reyes, Edwin N. Quiros, Determination of the Start and End of Combustion in a Direct Injection Diesel Engine Using the Apparent Heat Release Rate, ASME 2017 Power Conference Joint With ICOPE-17 collocated with the ASME 2017 11th International Conference on Energy Sustainability, the ASME 2017 15th International Conference on Fuel Cell Science, Engineering and Technology, and the ASME 2017 Nuclear Forum, Volume 1: Boilers and Heat Recovery Steam Generator; Combustion Turbines; Energy Water Sustainability; Fuels, Combustion and Material Handling; Heat Exchangers, Condensers, Cooling Systems, and Balance-of-Plant, POWER-ICOPE2017-3446, Charlotte, North Carolina, USA, June 26-30, 2017.

[11] T. Gao, S. Yu, K. Xie, M. Jeftic, M. Wang, M. Zheng, The Estimation of Nitrogen Oxides Reduction Potential Through Enhanced Heat Release Analysis, ASME 2016 Internal Combustion Engine Division Fall Technical Conference, ICEF2016-9440, Greenville, South Carolina, USA, October 9-12, 2016.

[12] P. Bares, D. Selmanaj, C. Guardiola, C. Onder, A new knock event definition for knock detection and control optimization, *Applied Thermal Engineering* 131 (2018) 80-88.

[13] A. Moosa, A. Farzad, A. Saeed, Z. Alireza, Classification-Based Fuel Injection Fault Detection of a Trainset Diesel Engine Using Vibration Signature Analysis, *Journal of Dynamics Systems, Measurement and Control* 142-5 (2020) 051003.

[14] Z. Yang, X. Han, S. Yu, X. Yu, M. Wang, M. Zheng, D. Ting, A Fuel Sensitive Ignition Delay Model for Direct Injection Diesel Engine Operating under EGR Diluted Conditions, SAE Technical Paper No. 2018-01-0231, 2018.

[15] R. Finesso, O. Marello, D. Misul, E. Spessa, M. Violante, Y. Yang, Gilles Hardy and Christian Maier, Development and Assessment of Pressure-Based and Model-Based Techniques for the MFB50 Control of a Euro VI 3.0L Diesel Engine, *SAE International Journal of Engines* 10 (2017) 1538-1555.

[16] Y. Yang, Z. Peng, W. Zhang, G. Meng, Parameterised Time-frequency Analysis Methods and Their Engineering Applications: A Review of Recent Advances, *Mechanical Systems and Signal Processing* 119 (2019) 182-221.

[17] Z. Feng, M. Liang, F. Chu, Recent Advances in Time–Frequency Analysis Methods for Machinery Fault Diagnosis: A Review with Application Examples, *Mechanical Systems and Signal Processing* 38 (2013) 165-205.

[18] G. Purushottma, T. Rajiv, Multifault Diagnosis of Induction Motor at Intermediate Operating Conditions Using Wavelet Packet Transform and Support Vector Machine, *Journal of Dynamics Systems, Measurement and Control* 140-8 (2018) 081014.

[19] A.Taghizadeh-Alisaraei, B. Ghobadian, T. Tavakoli-Hashjin, S. S. Mohtasebi, M. Azadbakht, Characterization of Engine's Combustion-Vibration Using Diesel and Biodiesel Fuel Blends by Time-frequency Methods: A Case Study, *Renewable Energy* 95 (2016) 422-432.

[20] S. Ji, X. Lan, J. Lian, H. Wang, M.Li, Y. Cheng, W. Yin, Combustion Parameter Estimation for ICE from Surface Vibration using Frequency Spectrum Analysis, *Measurement* 128 (2018) 485-494.

[21] J.M. Luján, C. Guardiola, B. Pla, P. Bares, Estimation of Trapped Mass by In-cylinder Pressure Resonance in HCCI Engines, *Mechanical Systems and Signal Processing* 66-67 (2016) 862-874.

[22] C. Guardiola, B. Pla, P. Bares, A. Barbier, An Analysis of the In-cylinder Pressure Resonance Excitation in Internal Combustion Engines, *Applied Energy* 228 (2018) 1272-1279.

[23] V. Dekys, P. Kalman, P. Hanak, P. Novak, Z. Stankovicova, Determination of Vibration Sources by Using STFT, *Procedia Engineering* 177 (2017) 496-501.

[24] A. Ferrari, F. Paolicelli, A Virtual Injection Sensor by Means of Time Frequency Analysis, *Mechanical Systems and Signal Processing* 116 (2019) 832-842.

[25] K. Ishiduka, K. Uchiyama, K. Higuchi, N. Yamada, K. Takeuchi, Herrmann OE, et al., Further Innovations for Diesel Fuel Injection Systems: Close-loop Control of Fuel Quantity by i-Art & Ultra High Injection Pressure, 19th Aachen colloquium, 2010.

[26] J.Hammer, M. Raff , D. Naber, Advanced Diesel Fuel Injection Equipment - A Never Ending BOSCH Story, 14th Internationales Stuttgarter Symposium, Springer Vieweg, Wiesbaden, Germany, 2014.

[27] P. Voigt, H. J. Schiffgens, C. Daveau, J. C. Oge, J. L. Beduneau, G. Meissonnier, C. Tapin, X. Lale, Delphi Injector Closed Loop Control Strategy Using the "Switch" Technology for Diesel Passenger Cars – Injector Hardware. 10. Tagung Diesel- und Benzindirekteinspritzung 2016. Wiesbaden: Springer

Vieweg; 2016. p. 41–66.

[28] A. Ferrari, C. Novara, E. Paolucci, O. Vento, M. Violante, T. Zhang, Design and Rapid Prototyping of a Closed-loop Control Strategy of the Injected Mass for the Reduction of CO2, Combustion Noise and Pollutant Emissions in Diesel Engines, *Applied Energy* 232 (2018) 358-367.

[29] A. Ferrari, C. Novara, E. Paolucci, O. Vento, M. Violante, T. Zhang, A New Closed-loop Control of the Injected Mass for a Full Exploitation of Digital and Continuous Injection-rate Shaping, *Energy Conversion and Management* 177 (2018) 629-639.

[30] A. Ferrari, T. Zhang, Benchmark between Bosch and Zeuch Method-Based Flowmeters for the Measurement of the Fuel Injection Rate, *International Journal of Engine Research* (2019) In press.

[31] A. E. Catania, A. Ferrari, E. Spessa, Temperature variations in the simulation of high-pressure injection-system transient flows under cavitation, *International Journal of Heat and Mass Transfer* 51 (2008), 2090-2107.

[32] Ferrari A., Mittica A., Thermodynamic formulation of the constitutive equations for solids and fluids, *Energy Conversion and Management* 66 (2016), 77-86.

[33] Payri, R., F. Salvador, M. Carreres and J. D. L. Morena. “Fuel temperature influence on the performance of a last generation common-rail diesel ballistic injector. Part II: 1D model development, validation and analysis.” *Energy Conversion and Management* 114 (2016): 376-391.

[34] F. J. Salvador, J. Gimeno, M. Carreres, M. Crialesi-Esposito, Fuel Temperature Influence on the Performance of a Last Generation Common-Rail Diesel Ballistic Injector. Part I: Experimental Mass Flow Rate Measurements and Discussion, *Energy Conversion and Management* 114 (2016), 364-375.

[35] C. Öztürk, Development of Experimental Techniques to Minimise the Leakage Errors Involved in FFT based Measurements, Applied Acoustics 44-4 (1995), 375-382.

[36] Ferrari, A. and O. Vento. “Influence of Frequency-Dependent Friction Modeling on the Simulation of Transient Flows in High-Pressure Flow Pipelines.” Journal of Fluids Engineering-transactions of The Asme, 142 (2020).

[37] Q. Fang, J. Fang, J. Zhuang, Z. Huang, Influences of Pilot Injection and Exhaust Gas Recirculation (EGR) on Combustion and Emissions in a HCCI-DI Combustion Engine, *Applied Thermal Engineering* 48 (2012) 97-104.

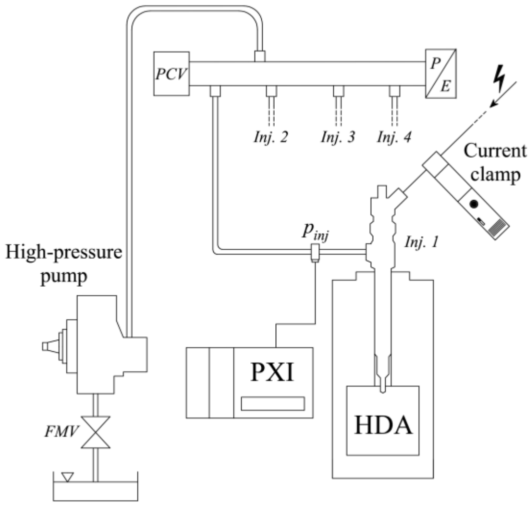

Figure 1. The experimental layout of the injection system

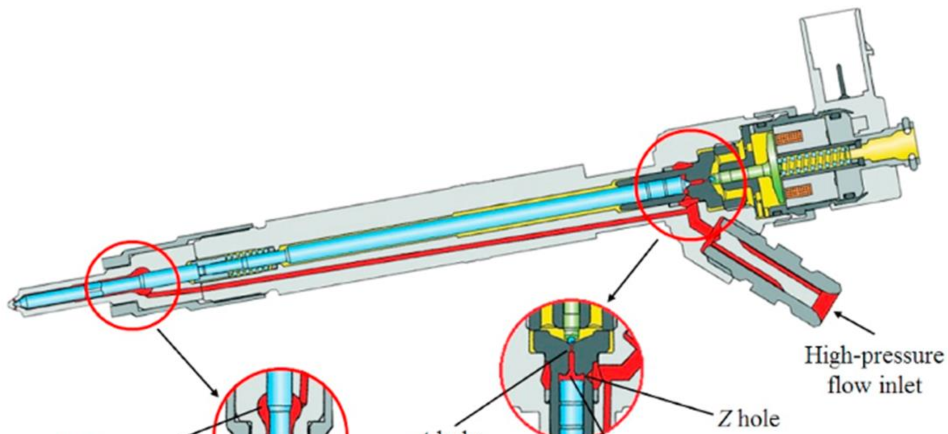

Figure 2. CRI 2.18 solenoid injector

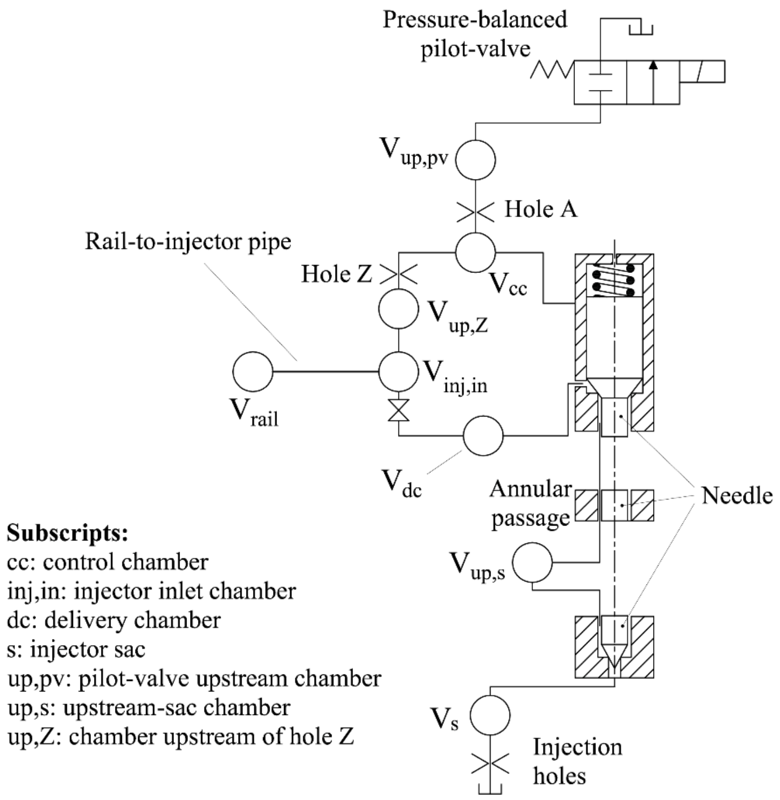

Figure 3. Schematic of the hydraulic circuit of the injection system

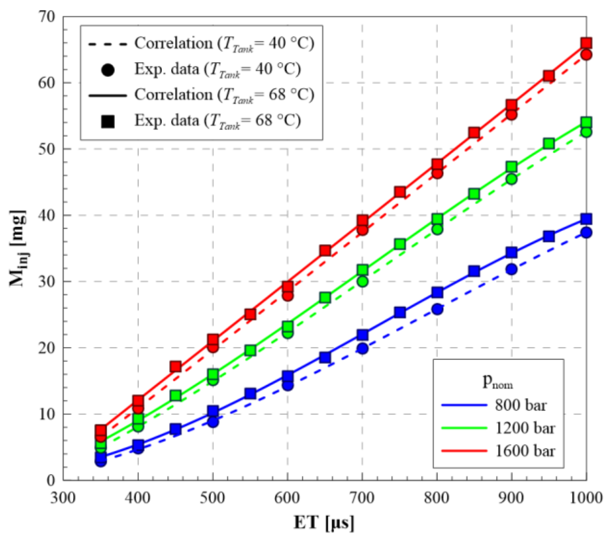

Figure 4. Injector characteristics for different p_{nom} and T_{tank} values

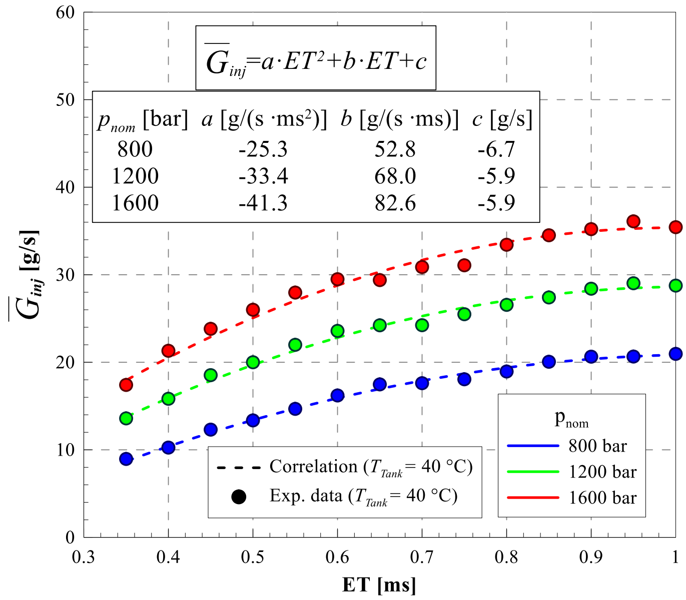

Figure 5. The mean injected flow-rate with respect to *ET* for different p_{nom} values

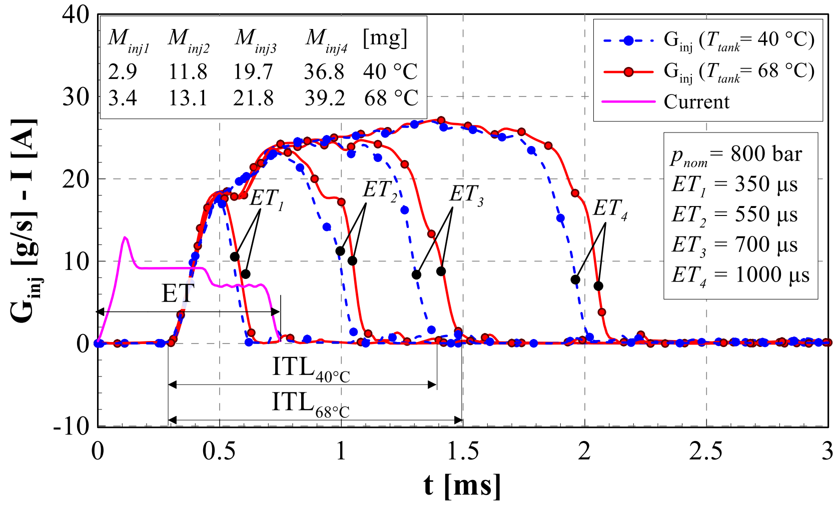

(a)

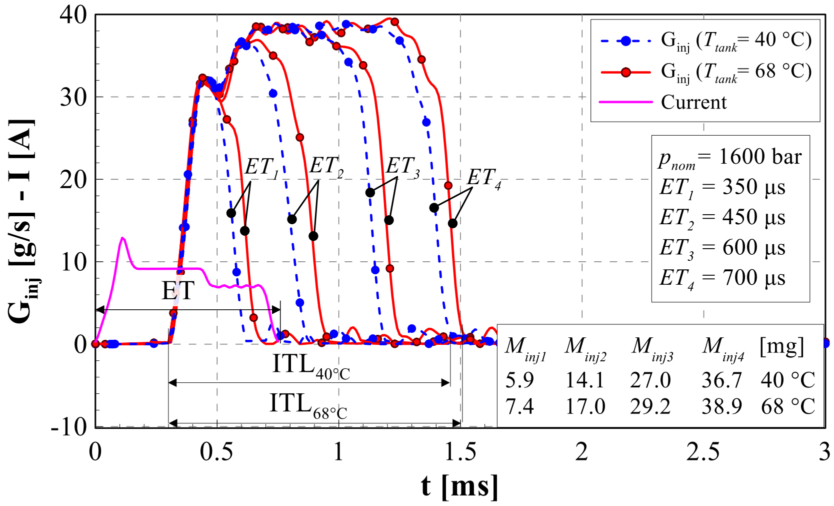

(b)

Figure 6. Effect of the tank fuel temperatures on the injected flow-rate for different *ET* values.

(a): p_{nom} = 800 bar (b): p_{nom} = 1600 bar

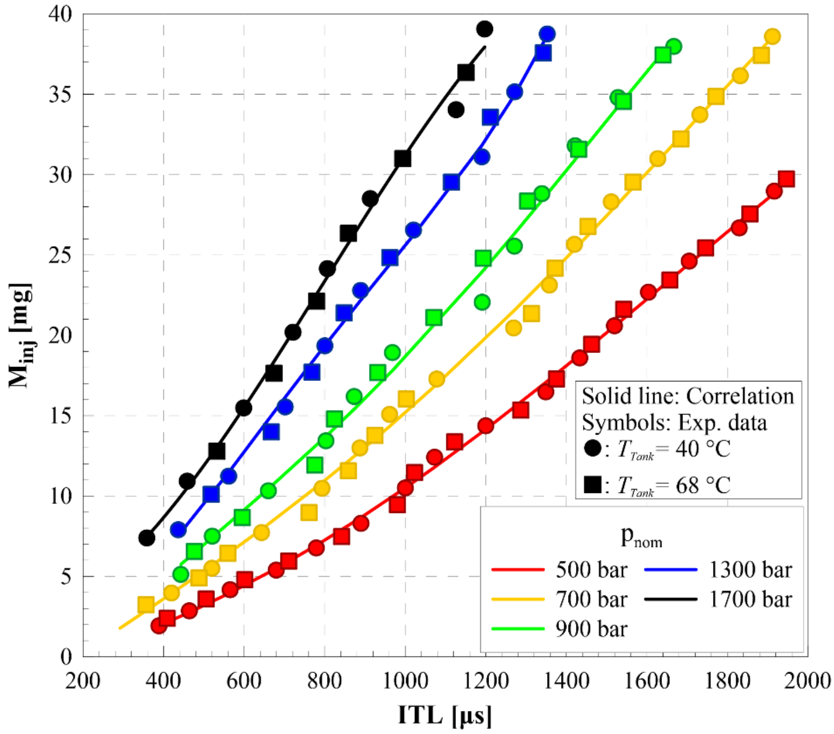

Figure 7. ***ITL-M$_{inj}$*** **injector characteristic for different** ***p_{nom}*** **and** ***T_{tank}*** **values**

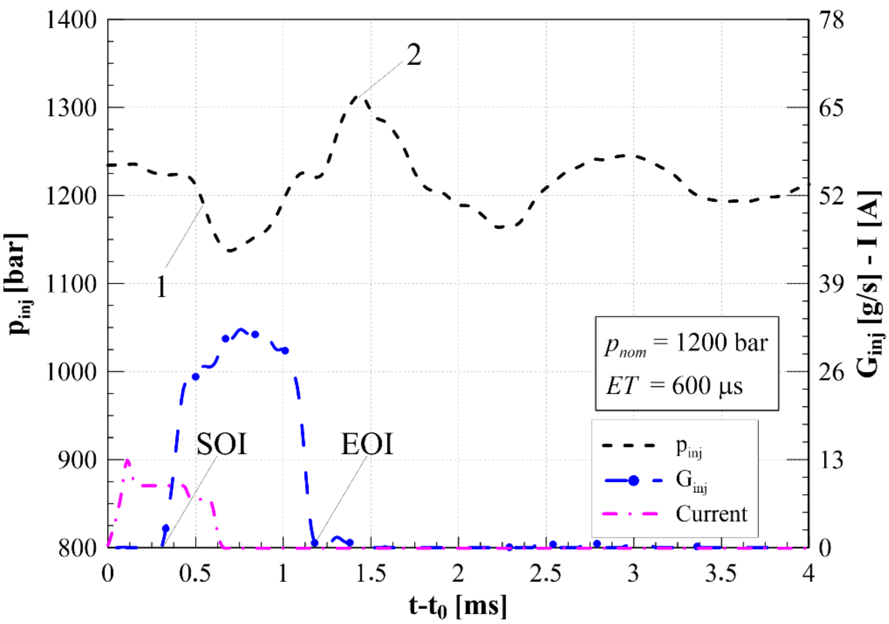

Figure 8. ***$G_{inj}(t)$*****,** ***$p_{inj}(t)$*** **and electrical current for** ***p_{nom}*****=1200 bar and** ***ET*****=600 µs**

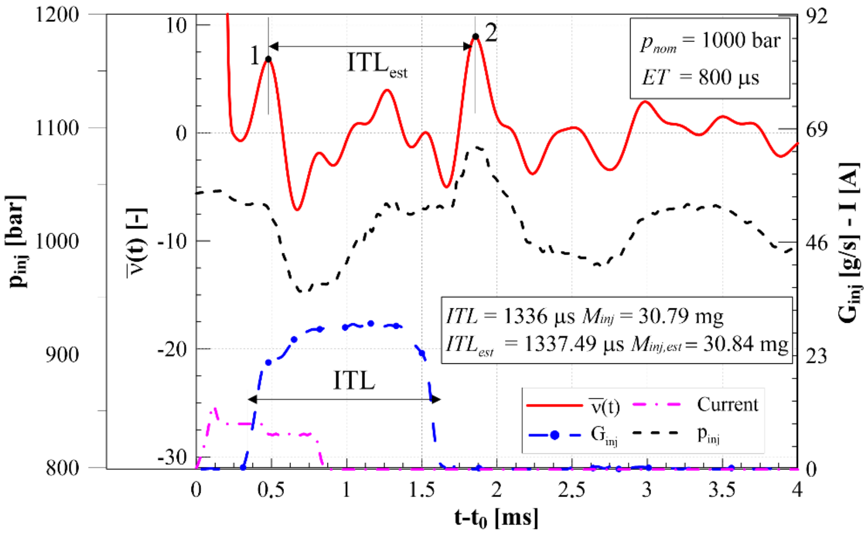

Figure 9. ***$G_{inj}(t)$*, *$p_{inj}(t)$* and the normalized *MIF* for *p_{nom}*=1000 bar and *ET*=800 μs (*T_{tank}*=40 °C)**

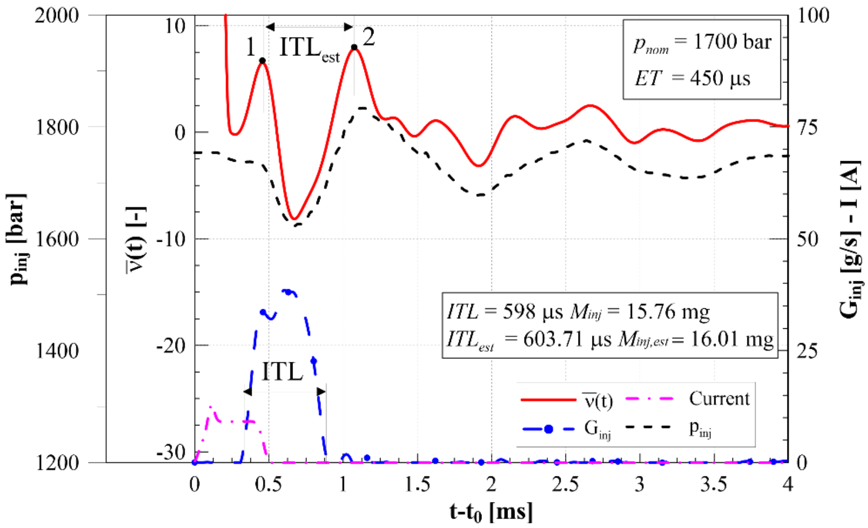

Figure 10. ***$G_{inj}(t)$*, *$p_{inj}(t)$* and the normalized *MIF* for *p_{nom}*=1700 bar and *ET*=450 μs (*T_{tank}*=40 °C)**

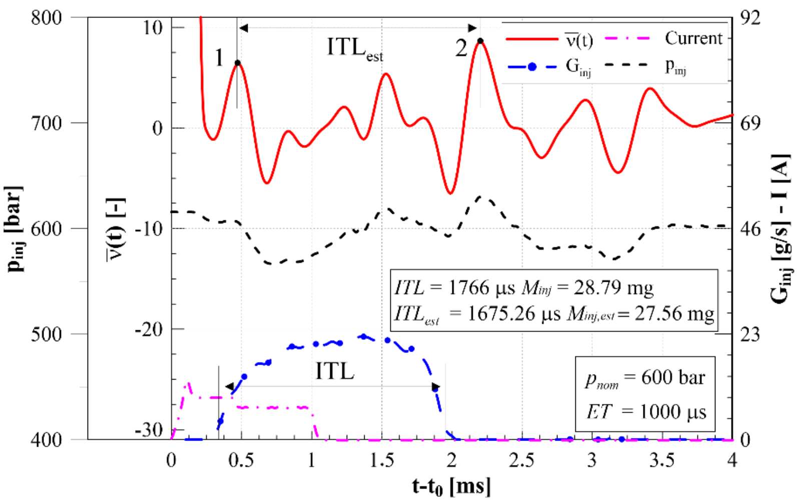

Figure 11. ***$G_{inj}(t)$*, *$p_{inj}(t)$* and the normalized *MIF* for *p_{nom}*=600 bar and *ET*= 1000 μs (*T_{tank}*=40 °C)**

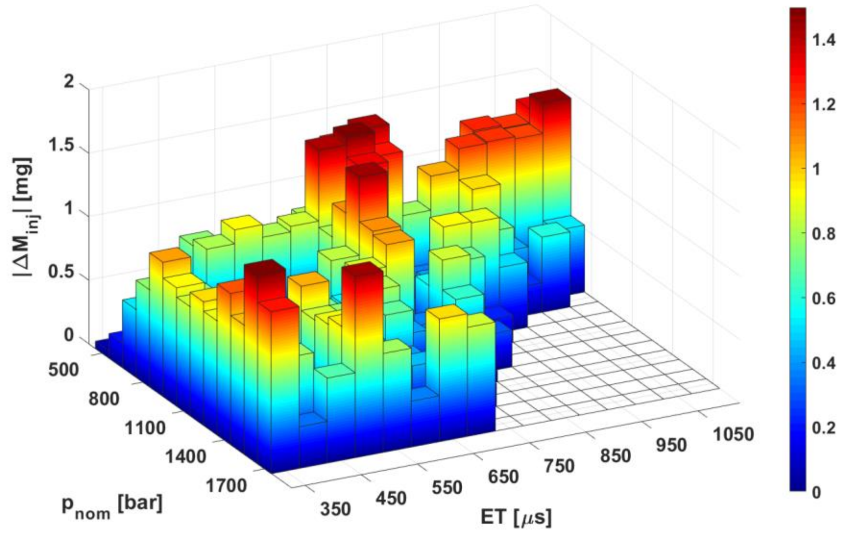

(a)

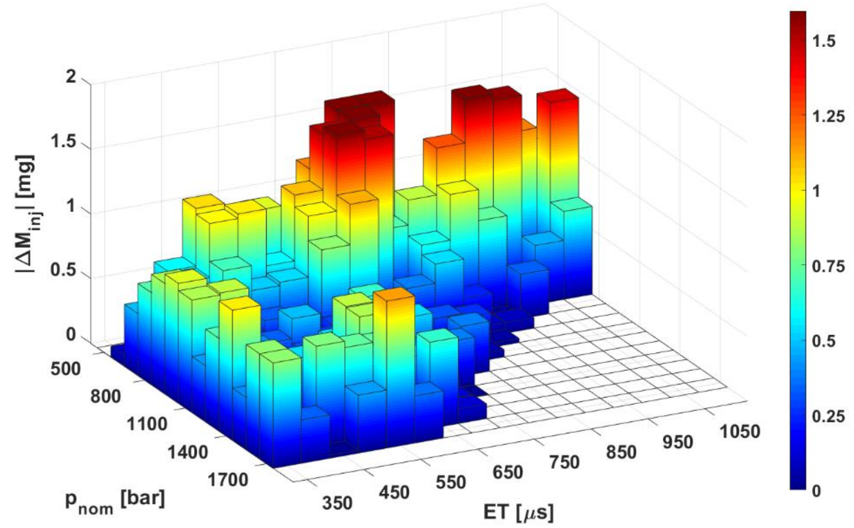

(b)

Figure 12. Injected mass prediction accuracy (*a*: T_{tank}= 40 °C, *b*: T_{tank}= 68 °C)

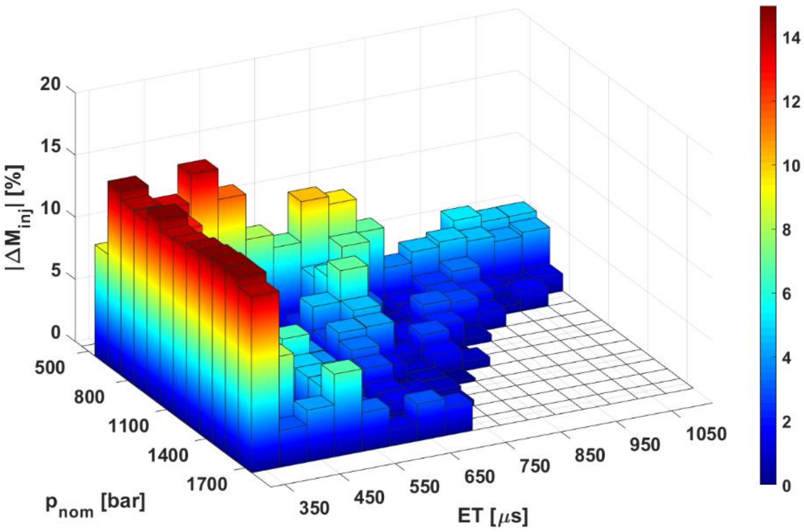

(a)

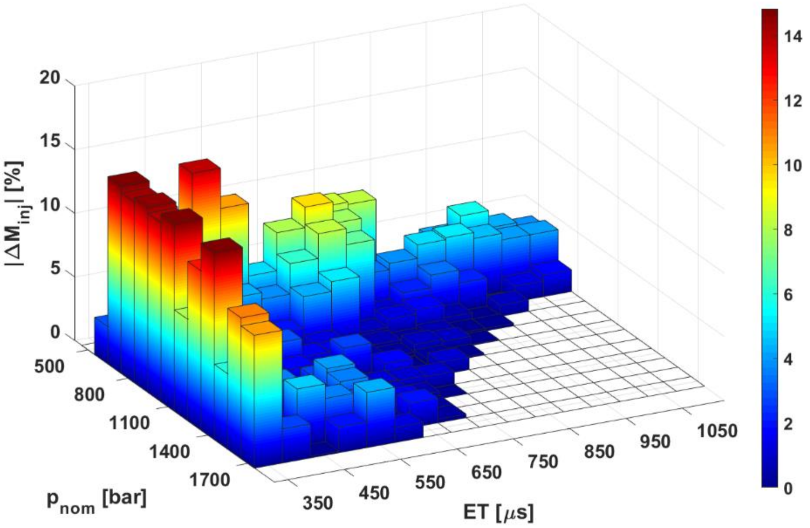

Injected mass prediction percentage error (*a*: T_{tank}= 40 °C, *b*: T_{tank}= 68 °C)

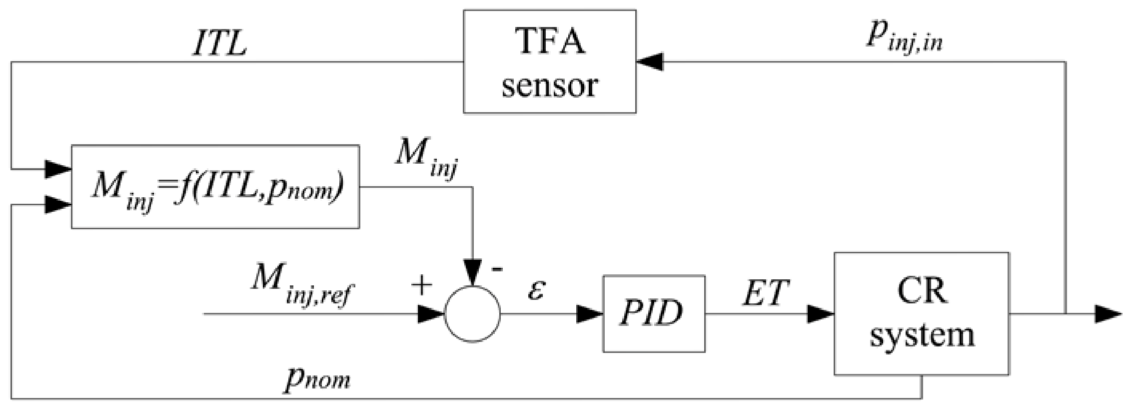

Figure 14. The implemented closed-loop strategy based on *TFA* analysis